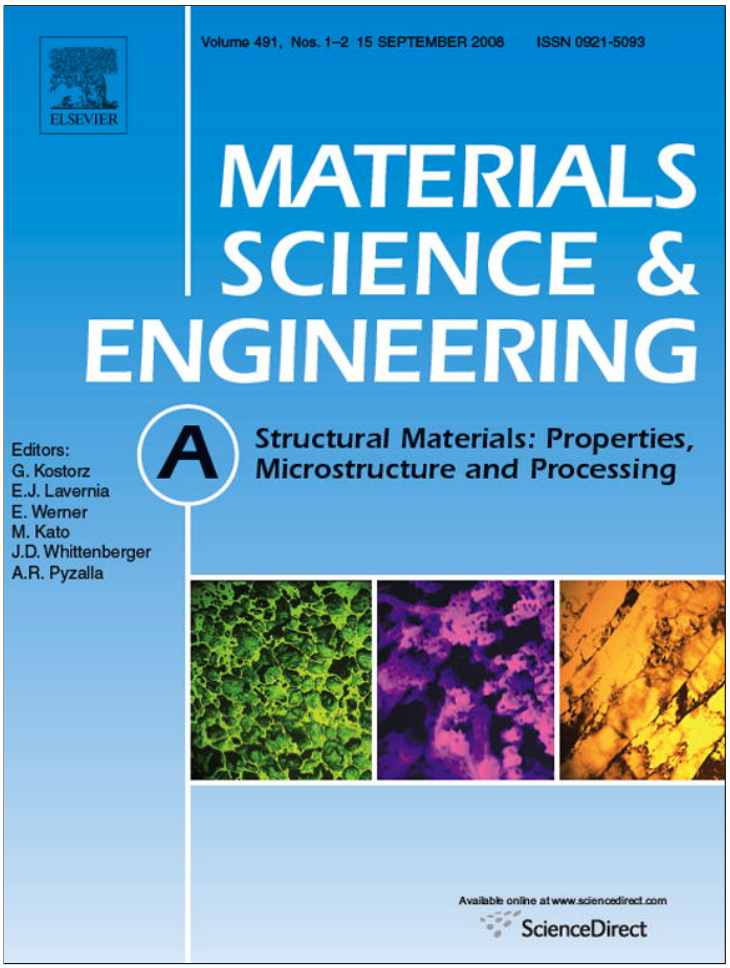

Materials Science and Engineering A 491 (2008) 214–223

Contents lists available at ScienceDirect

Materials Science and Engineering A

journal homepage: www.elsevier.com/locate/msea

The effect of silver on microstructural evolution in two 2xxx series Al-alloys with a high Cu:Mg ratio during ageing to a T8 temper

D. Bakavos [a], P.B. Prangnell [a,*], B. Bes [b], F. Eberl [b]

[a] Materials Science Centre, School of Materials, The University of Manchester, Grosvenor Street, Manchester M1 7HS, UK
[b] Alcan International, Centre de Recherche Voreppe, B.P. 27, 725 rue Aristide Bergès, 38340 Voreppe, France

ARTICLE INFO

Article history:
Received 19 September 2007
Received in revised form 25 January 2008
Accepted 13 March 2008

Keywords:
Aluminium alloys
Al–Cu–Mg
Al–Cu–Mg–Ag
High Cu:Mg ratio
Internal stresses
Ω phase
σ phase
Ag additions

ABSTRACT

The precipitation behaviour in two high Cu:Mg ratio 2xxx series Al-alloys, 2022 and 2139, has been investigated in detail during artificial ageing to a T8 temper; the main difference in composition between the two alloys being a ~0.3% silver addition in 2139 and a slightly higher Mg level. The addition of Ag in 2139 lead to enhanced ageing kinetics and a significant increase in strength, due to promotion of the Ω phase, which became the dominant age hardening precipitate. Some Ω was also observed in the Ag-free 2022 alloy, although Ω precipitation has not been previously reported in 2xxx series alloys with such low Mg levels. The S and σ phase were also found to nucleate heterogeneously as minor constituents in both alloys, although the size of the σ phase was reduced in the Ag bearing alloy. Finally, the weak remaining residual stresses in thick plate material, after stretching, were found to bias the habit plane selection of Cu GP zones and the θ″ metastable phases in the 2022 material, but had no effect on the Ω phase predominantly present in 2139.

1. Introduction

2xxx series Aluminium alloys, like the high Cu to Mg ratio Al–Cu–Mg 2022 and silver containing Al–Cu–Mg–Ag 2139 compositions, have only recently become commercially available and are under development as potential precipitation hardened materials for damage tolerant applications in the aerospace industry [1,2]. The aim of this research is to offer a substantially higher proof strength in an artificially aged T8 temper with similar levels of damage tolerance, compared to traditionally used naturally aged alloys, like 2 × 24-T3. In addition, alloys in this composition range have the added advantage of good weldability and when artificially aged are more compatible with low cost integrated manufacturing routes, such as the creep-ageforming of laser-welded panels [3]. The main essential difference between the 2022 and 2139 compositions is the addition of ~0.3 wt.% silver in 2139, which also has a slightly higher Mg level (see Table 1). Overall, for aerospace applications silver containing alloys are more desirable, due to their higher strength and excellent thermal stability, but they are more expensive and difficult to creep-form [4–7].

The advantages that alloys like 2022 and 2139 offer, relative to more conventional Mg rich 2xxx series aerospace alloys, such as the 2×24 variants, are mainly based on the alternative precipitation sequences they exhibit during artificial ageing [1]. Although the precipitation behaviour in these specific alloys has not been previously studied in detail, a high Cu:Mg ratio leads to the promotion of plate-shaped Cu GP zones and Al_2Cu-based transition phases θ′, whereas above a minimum Mg level the inclusion of Ag promotes Ω precipitation [7–13]. In comparison low Cu:Mg ratios favour the formation of Cu–Mg co-clusters and strengthening on artificial ageing through the semicoherent orthorhombic S′ or S (Al_2CuMg) phase and its possible precursor S″/GPB2 [14–16].

From evidence in the literature [7–13], the Cu:Mg ratio in the ternary Al–Cu–Mg system should exceed ~5.6:1 in order for the thin plate Al_2Cu, θ and Ω phases to dominate on $\{1\,0\,0\}_{Al}$ and $\{1\,1\,1\}_{Al}$ habit planes, respectively, and minimise the presence of the less desirable, in terms of the alloy's all-round mechanical performance, S′/S phase. The tetragonal Ω phase is particularly advantageous because, by precipitating as plates in high densities on $\{1\,1\,1\}_{Al}$ planes, it promotes a higher yield strength by interacting more strongly with glide dislocations than θ′, without encouraging shear localisation [17,18]. As Ω is probably a coherent form of the equilibrium θ phase, it is also more stable than θ′ [5,6,11–13]. Ω is thought to nucleate from Cu–Mg, or Cu–Mg–Ag, co-clusters and Mg and Ag then segregates to its interface to reduce its coherency misfit strain [11–13]. It is thus usually considered that a

* Corresponding author. Tel.: +44 161 306 3610; fax: +44 161 306 3586.
E-mail addresses: dimitrios.bakavos@manchester.ac.uk (D. Bakavos), philip.prangnell@manchester.ac.uk (P.B. Prangnell), bernard.bes@alcan.com (B. Bes), frank.eberl@alcan.com (F. Eberl).

0921-5093/$ – see front matter © 2008 Elsevier B.V. All rights reserved.
doi:10.1016/j.msea.2008.03.014

Table 1
Compositions and ageing treatments of the materials investigated

Material type	2022	2139
Composition (wt.%)	4.84 Cu, 0.21 Mg, 0.4 Mn 0.02 Si, 0.05 Fe	4.83 Cu, 0.40 Mg, 0.35 Ag, 0.29 Mn, 0.06 Si, 0.07 Fe
T851 temperature	24 h at 173 °C	16 h at 175 °C
% Stretch	2–3	2–3

Mg content of greater than ~0.3 wt.% is required for Ω precipitation [9–13]. Because of the low Mg level (Table 1), the Ω phase would not normally be expected to develop in the silver-free 2022 alloy under investigation. The Mg:Si ratio also plays a role in influencing Ω precipitation and, according to Gable et al. [9], in the absence of Ag should be greater than two for Ω to form.

In certain circumstances it is known that residual stresses can influence the precipitation behaviour in Al–Cu–Mg–(Ag) alloys containing thin plate-shaped precipitates [19]. The negative plate normal coherency strains associated with, Cu GP zones, θ″, θ′ and Ω precipitates, have all been shown to interact with far-field stresses, which can bias their habit plane variant selection and size [20–23]. For example, all of the precipitates listed above will nucleate preferentially on habit plane variants parallel to a tensile, or perpendicular to a compressive, stress axis to relax their negative coherency misfit [20]. By artificially applying external stresses it has been shown that the tensile stress threshold for precipitate alignment is of the order of only 20 MPa for θ′, and is probably lower for its precursors θ″ and $\{0\,0\,1\}_{Al}$ habit plane Cu GP zones [20–23], which is of a similar magnitude to the residual stresses retained in thick plate products after quenching and stretching [24]. In comparison, the threshold stress for Ω is considerably higher being at least 120 MPa [22].

The main objective of this study was to investigate, in more detail than previously the precipitate evolution that takes place during artificial ageing of the new high Cu–Mg ratio 2xxx aerospace alloys, 2022 and 2139. Of particular interest was to understand whether in the absence of silver the Ω phase could form in alloys like 2022 with such low Mg contents, and to identify other minor phases that might appear, apart from the expected main strengthening phases. The importance of other subtle effects, such as the influence of residual stresses and interactions between silver and the minor phases present was also of interest.

2. Experimental

The 2022 (Al–Cu–Mg) and 2139 (Al–Cu–Mg–Ag) 2xxx series aluminium alloys investigated were supplied by Alcan CRV as 40 mm plate and 5 mm sheet, in a T351 condition, following solution treatment and stretching by 2%. The compositions of the two alloys were selected to be mid range within the registered specification and are given in Table 1. They differ significantly only in terms of the silver content and the slightly higher Mg level in 2139. Both alloys contained similar levels of the dispersoid-forming element Mn, which has little influence on their relative artificial ageing behaviour. The recommended T851 ageing treatments used are also given in Table 1. All heat treatments were carried out in the same air circulating furnace, with an attached thermocouple, using a heating ramp of 75°/h. Samples were examined by TEM after different ageing times in a Philips CM200 and an FEI Tecnai F30, with EDX and STEM facilities, in order to image and chemically analyse the precipitates of interest. For STEM analysis a spot size of 2 nm was employed. TEM samples were prepared from the mid plane of each rolled plate by electropolishing with a 30% nitric acid methanol solution at −30 °C. TEM samples were viewed in the plate normal direction. The rolling direction (RD) was identified by scribing the rim of each disc and the alignment of dispersoids within the TEM foils. Four to six foils were investigated for each condition. Image analysis was used in order to measure the precipitate dimensions from TEM images. Age hardening curves for both the alloys were measured using a Vickers hardness machine, with an applied load of 20 kg.

3. Results and discussion

3.1. General age hardening behaviour

Comparison of the ageing curves (Fig. 1) for the two alloys aged to their respective T8 tempers (see Table 1), indicates that the 2139 alloy has only a slightly higher initial hardness (~5 HV) in the original T351 condition, but there is a substantial difference in peak hardness as well as the ageing kinetics between the two alloys. Both alloys exhibited some reversion during the heating ramp with a similar loss of strength, of ~18 HV. However, the 2139 alloy showed both faster ageing kinetics and, a higher hardness than 2022, with an initial hardening rate double that of the silver-free alloy. The difference in hardness between the two alloys when peak aged can be attributed to the small silver addition and slightly higher Mg level promoting a high density of Ω $\{1\,1\,1\}_{Al}$ precipitation, at the expense of θ″/θ′ $\{0\,0\,1\}_{Al}$, in the 2139 alloy (see below). Thin Ω plates on $\{1\,1\,1\}_{Al}$ habit planes have been shown to act as stronger obstacles to glide dislocations than $\{0\,0\,1\}_{Al}$ plates, or rod or lath-shaped precipitates, and are more effective at increasing yield strength and reducing shear localisation [17,18].

The marked difference in early stage ageing kinetics from the addition of silver, is not just due to the slightly higher recommended ageing temperature for 2139 (175 compared to 173 °C), but has also been noted by several other research groups [5–13,25,26]. This effect has been previously attributed to the strong tendency of Ag to bind quenched in vacancies and lead to the faster formation of Mg–Ag and Mg–Ag–Cu co-clusters, relative to Cu GP zones and Cu–Mg clusters, which promotes nucleation of the Ω (Al_2Cu) phase [13]. As ageing progresses, it is thought that Cu–Mg–Ag plate-shaped clusters, or GP zones with a $\{1\,1\,1\}_{Al}$ habit plane,

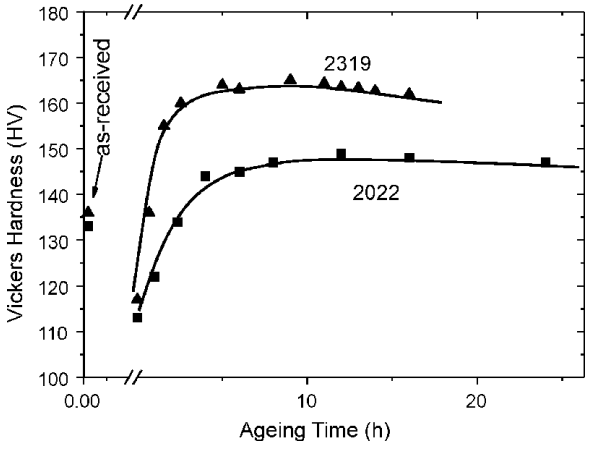

Fig. 1. Age hardening curves for the 2022 (Al–Cu–Mg) and the 2139 (Al–Cu–Mg–Ag) alloys during their respective T8 heat treatments.

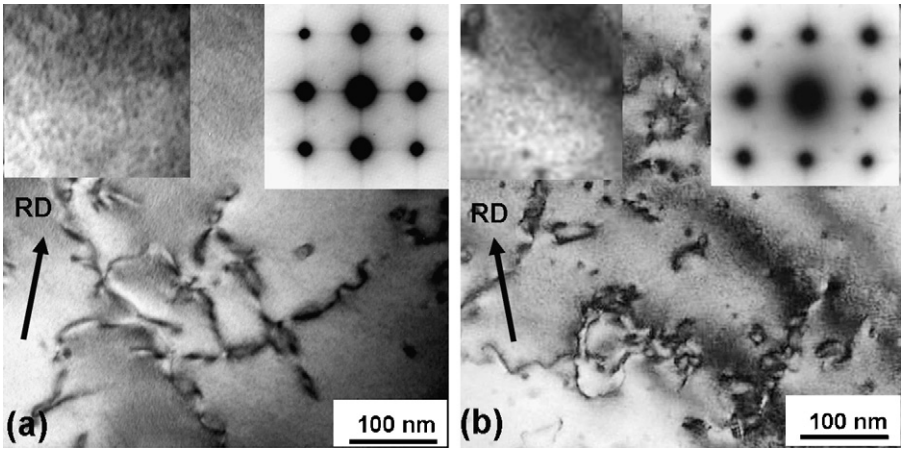

Fig. 2. TEM images and diffraction patterns for the naturally aged T351 condition, near a $\langle 0\,0\,1\rangle_{Al}$ zone axis, showing dislocations and in the magnified insert background strain contrast, in (a) for 2022 and (b) 2139. Note the stronger strain contrast and $\langle 0\,0\,1\rangle$ streaking in the diffraction pattern for the 2022 alloy.

develop from the co-clusters formed on natural ageing that survive reversion and act as precursors for the Ω (Al_2Cu) plate-shaped precipitates [12]. This also leads to a higher overall hardness increase relative to that found in θ″ or S dominated microstructures [7–12,14–16].

The phases formed in the alloys during ageing will be discussed sequentially in more detail in the following sections.

3.2. T351 as received condition

Fig. 2 shows BF images and SAED patterns for the 2022 silver-free and 2139 silver-containing alloys (of otherwise identical composition) in the initial solution treated stretched and naturally aged T351 condition, taken close to a $\langle 0\,0\,1\rangle_{Al}$ zone axis. Even in this naturally aged state, the influence of the addition of a small concentration of silver can be seen in the TEM images and diffraction data. The BF images reveal strain contrast associated with a high density of dislocations generated during the 2% stretching operation. In the magnified inserts finer scale mottled background strain contrast is also present, as well as weak $\langle 0\,0\,1\rangle_{Al}$ streaking in the diffraction patterns. It can be noted that the strain contrast and streaking is much stronger for the silver-free 2022 alloy (Fig. 2a), indicating the presence of Cu GP zones on $\{0\,0\,1\}_{Al}$ habit planes. The less pronounced streaking, and weaker strain contrast in the silver containing 2139 alloy (Fig. 2b) is a result of the tendency of Ag to bind quenched in vacancies and form Mg–Ag and Mg–Ag–Cu co-clusters, leaving fewer Cu atoms available for forming $\{0\,0\,1\}_{Al}$ habit plane GP zones.

3.3. Early stage artificial ageing

Immediately after the end of the initial heating ramp, on reaching their respective ageing temperatures, the precipitation behaviour within the 2022 and 2139 alloys can be seen in the TEM data in Fig. 3. With the 2022 alloy (Fig. 3a) Strong $\langle 0\,0\,1\rangle_{Al}$ streaks can be seen in the SAD pattern that now contain weak intensity maximum, which is generally interpreted as coinciding with the appearance of θ″ [27]. At this early point in the artificial ageing sequence the 2022 alloy (Fig. 3a) thus contains a mixture of θ″ and coarser GP zones that survived reversion, from which θ″ develops [27–29]. When viewed in the same orientation, the 2139 alloy (Fig. 3b) again shows less evidence of Cu $\{0\,0\,1\}_{Al}$ GP zone and θ″ formation, with a very low density of $\langle 0\,0\,1\rangle$ orientated plates seen in the image and far weaker streaking in the diffraction pattern (note a longer exposure was used relative to Fig. 3a). No clear evidence of Ω formation was found at this stage of artificial ageing.

In this early aged condition, somewhat surprisingly, the θ″ plates and Cu $\{0\,0\,1\}_{Al}$ GP zones in the stretched thick Plate 2022 material were found to be preferentially aligned, parallel to the rolling direction. This effect can be clearly seen in Fig. 3a, where when viewed

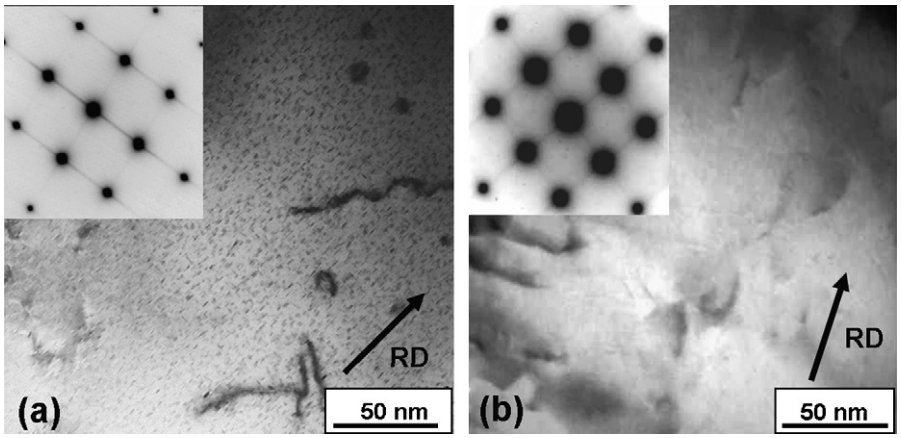

Fig. 3. Bright field TEM micrograph, close to a $\langle 0\,0\,1\rangle_{Al}$ zone axis, and corresponding SAED $\langle 0\,0\,1\rangle_{Al}$ diffraction patterns, for (a) the 2022 and (b) the 2139 alloy aged 0.01 h at 173 °C.

near the $\langle 0\,0\,1\rangle_{Al}$ zone axis, there should be two mutually perpendicular $\{0\,0\,1\}_{Al}$ habit plane variants lying edge on to the plane of the foil, with a third lying in the plane of the foil that cannot be easily seen with this orientation. However, in the image one set of GP zones/θ″ discs, lying edge on to the foil and close to parallel to the rolling direction, dominates. In the SAED pattern insert stronger streaking is also seen in the $\langle 0\,0\,1\rangle_{Al}$ direction ~ normal to RD. This effect will be discussed further below (Section 3.4).

The precipitation behaviours seen in the two alloys after ageing for ~2.5 h at temperature are shown in Fig. 4. In the 2022 alloy (Fig. 4a) θ′ has now begun to nucleate heterogeneously on dislocations, while the homogenously nucleated GP zones have developed into θ″ within the dislocation-free volumes of the material. For the same ageing time (Fig. 4b and c), TEM images from the 2139 alloy (aged 2° higher at 175 °C) revealed that the microstructure also contained some θ′ nucleated heterogeneously on dislocations, but the background matrix now consisted predominantly of fine Ω plates. The Ω plates can be seen more clearly from the $\langle 0\,1\,1\rangle$ orientated image in Fig. 4c. In the $\langle 0\,0\,1\rangle$ zone axis diffraction pattern (Fig. 4b) a set of four spots characteristic of Ω reflections from the four $\{1\,1\,1\}_{Al}$ habit plane variants, symmetrically opposed on diagonals surrounding the $0\,1\,1_{Al}$ position at 1/3 $\{0\,1\,1\}_{Al}$ 2/3 $\{0\,1\,1\}_{Al}$ [30], were also seen for the first time, all be it relatively weakly (enlarged in Fig. 5b). These results are broadly in line with the age hardening curves, discussed above, which showed enhanced early stage ageing kinetics for 2139 due to microalloying with Ag.

3.4. Peak ageing and the T8 condition

On further ageing the 2022 alloy 10 h at temperature (173 °C), the peak hardness plateau was reached (Fig. 1). In this condition the microstructure was found to consist predominately of a high density of θ″ in the background matrix, with a lower density of dislocation nucleated θ′ (Fig. 5a). It is well established that maximum hardness in ageing curves for binary Al–Cu alloys occurs with a mixture of coherent θ″ and semicoherent θ′ plates [31]. Surprisingly, given the low Mg level (0.2 wt.%) and lack of Ag, a low density of Ω (Al_2Cu) precipitates was observed in the 2022 alloy for this ageing condition, shown more clearly in the $\langle 0\,1\,1\rangle$ orientated insert in Fig. 5a. A weak set of four Ω reflections could also be seen surrounding the $0\,1\,1_{Al}$ position (enlarged area of the $\langle 0\,0\,1\rangle$ diffraction pattern in Fig. 5a). In addition, a very low volume fraction of S (Al_2CuMg) phase was found to have formed, indicated by arrows in the enlarged image in Fig. 5a. This phase was identified from its morphology, $\{0\,1\,2\}_{Al}$ habit plane orientation, and the presence of Mg and Cu, via STEM analysis.

The 2139 alloy reached peak hardness after around ~6 h at temperature (175 °C). After this ageing time the microstructure consisted mainly of fine Ω plates, which had developed further in size relative to the underaged condition, and some θ′. The θ′ phase was only seen on dislocations (Fig. 5b). A very small volume fraction of S phase was also found, with a similar density to in the Ag-free 2022 alloy. No evidence of σ phase was seen at this stage in either alloy.

On ageing the 2022 alloy 24 h to the final full T8 temper, θ′ became the dominant strengthening phase and little θ″ remained (Fig. 6a and b), as can also be seen form the diffraction patterns which contain reflections primarily form the three $\{0\,0\,1\}_{Al}$ habit plane variants of the θ′ phase. θ′ mainly nucleated heterogeneously on dislocation networks in the stretched alloy, but was also present in dislocation-free regions. It is now generally recognised that θ′ does not form by transformation of θ″, but nucleates independently, largely heterogeneously at dislocations [32–34], and consumes the less stable metastable coherent θ″ phase as ageing progresses. It is also possible for θ′ to nucleate via an autocatalytic mechanism

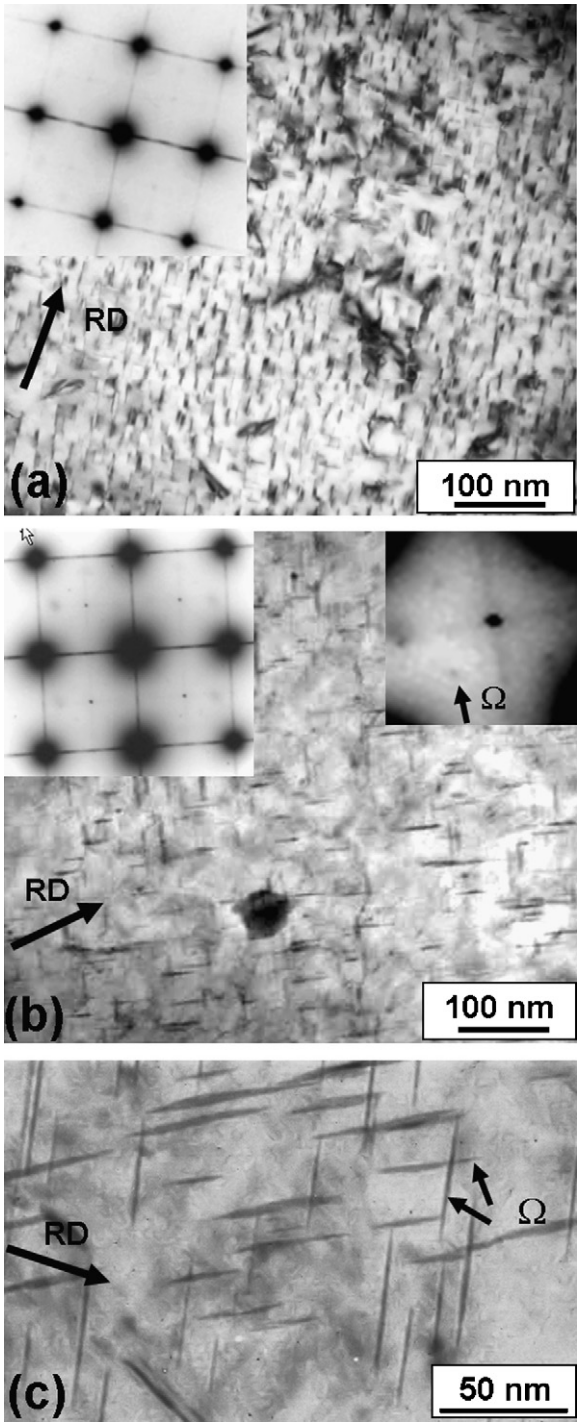

Fig. 4. Bright field TEM micrographs, close to a $\langle 0\,0\,1\rangle_{Al}$ zone axis, and corresponding SAED $\langle 0\,0\,1\rangle_{Al}$ diffraction patterns, for (a) the 2022 and (b) the 2139 alloy after ~2.5 h at 173 °C, and in (c) the 2139 alloy close to a $\langle 1\,1\,0\rangle_{Al}$ zone axis, revealing the Ω phase. The enlarged SAED region highlighted in (b) is from around the $1\,1\,0_{Al}$ position.

[35] and in some circumstances at the θ″/Al matrix interface [36]. Although in the majority of the 2022 thick plate material θ′ precipitates were randomly distributed over the three possible $\{0\,0\,1\}_{Al}$ habit plane variants (e.g. Fig. 6a), some areas of local θ′ precipitate alignment, parallel to the plate longitudinal tensile residuals stresses, were still found in the T8 condition (see Fig. 6b).

During ageing the 2022 alloy to the full T8 temper the Ω phase increased in volume fraction, as can be seen from the higher inten-

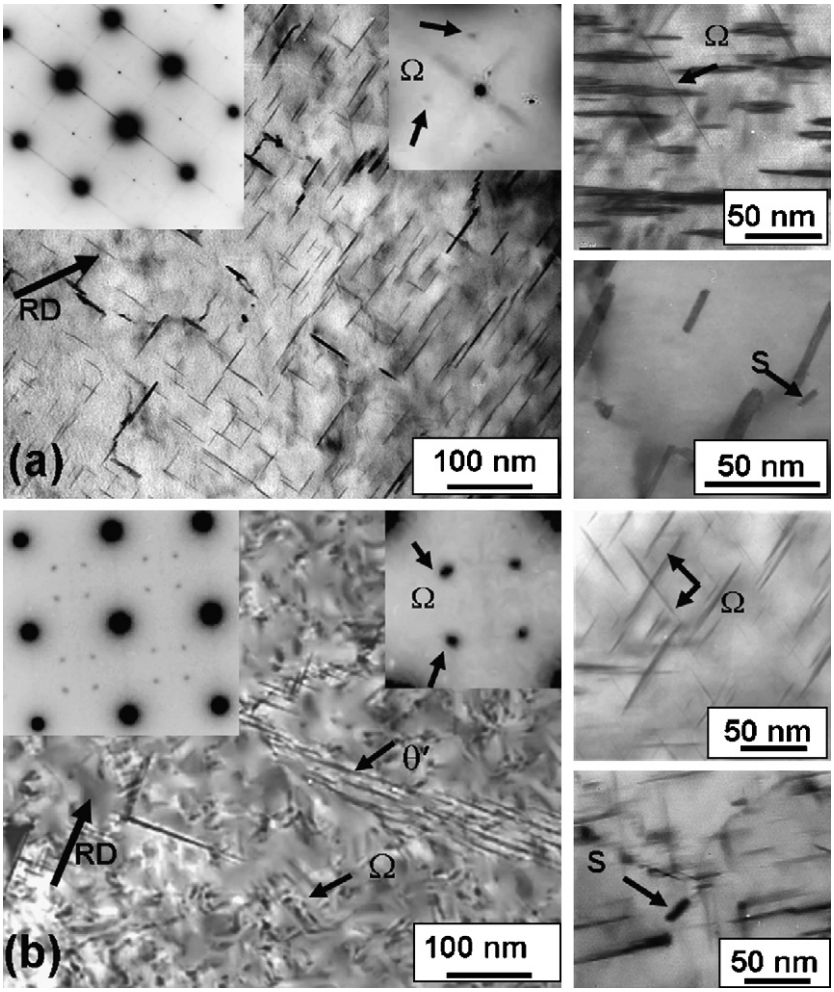

Fig. 5. TEM micrographs and diffraction data close to a $\langle 1\,0\,0\rangle_{Al}$ zone axis after reaching peak hardness shows (a) the θ″ and θ′ phases predominantly found in the 2022 alloy (10 h at 173 °C) with examples of minor phases Ω and S, enlarged, and (b) the Ω phase predominantly found in the 2139 alloy (6 h at 175 °C). Note the insert highlighting the Ω phase is tilted to an $\langle 0\,1\,1\rangle_{Al}$ zone and the enlarged regions from the $\langle 0\,0\,1\rangle_{Al}$ SAED patterns around the $1\,1\,0_{Al}$ position reveal the intensity of the four Ω reflections.

sity of its four spots around the $1\,1\,0_{Al}$ position in Fig. 6a, although it remained a minor component of the microstructure. The results thus suggest that Mg levels as low as 0.2 wt.% are sufficient to promote nucleation of the Ω phase, even in a Ag-free low Si content Al–Cu–Mg alloy like 2022. The formation of Ω in a Ag-free alloys with such low Mg levels has not been previously reported, with the exception of the work of Gable et al. [9] who studied the role of Si content. A minimum Mg level is known to be critical for Ω formation in Al–Cu–Mg alloys [9], but the evidence here suggests that the required level must be slightly lower than conventionally thought. Unfortunately, the nucleation mechanism of Ω in silver-free 2xxx series alloys is not yet well understood. For example, although Mg and Mg–Cu co-clusters can form during early ageing, there is yet no direct evidence they act as precursors for the Ω phase without the presence of Ag [11–13,14,15].

In the 2139 Al–Cu–Mg–Ag alloy, on ageing to the T8 temper, the Ω phase continued to develop, while the volume fraction of θ′ did not greatly increase above that seen after its earlier dislocation nucleation (Fig. 6c and d). The main strengthening phase at the end of the T8 ageing treatment was, therefore, Ω. Comparison of Fig. 6a and c, and the relative diffraction spot intensities in the enlarged diffraction pattern inserts, between the θ′ streaks in the two $\langle 1\,0\,0\rangle_{Al}$ directions and the four Ω reflections around the $1\,1\,0_{Al}$ position, shows that the minor addition of silver and slightly higher Mg level has greatly increased the density of Ω plates, which has now become the dominant precipitation phase largely replacing the θ′ precipitates seen in the 2022 alloy. This is confirmed in Fig. 6e and f, where the densities of Ω and θ′ precipitates are compared in 2022 and 2139 using dark field. The Ω and θ′ precipitates in the Ag-containing alloy are also finer compared to the same precipitates present in the Ag-free alloy, which may be partly due to the shorter T8 heat treatment. However, with the Ω phase a higher nucleation rate results from the strong interaction of Ag with excess vacancies and Mg, which provide precursory co-clusters and thus a higher homogeneous nucleation site density, without the requirement for dislocation nucleation [13]. The smaller size of the θ′ precipitates (plate length 38 nm as opposed to 70 nm in 2022) is presumably because they are in competition with the more stable Ω phase for solute and only appear by virtue of the early nucleation advantage they achieve by precipitating on dislocations where, once formed, they are unable to grow as extensively.

In the 2022 alloy the semicoherent lath morphology S phase was found to develop further on increasing the ageing time from 10 to 24 h, but remained at a very low volume fraction (Fig. 8). An additional phase, the tetragonal σ ($Al_5Cu_6Mg_2$) precipitate with a cuboidal morphology, not seen after 10 h ageing, was also observed at the end of the T8 temper in the 2022 alloy (Fig. 10a). This phase has previously only been reported [37–39] in alloys with higher Mg levels. In the T8 condition similar levels of S phase were found in the both materials. However, the cuboidal-shaped σ ($Al_5Cu_6Mg_2$) pre-

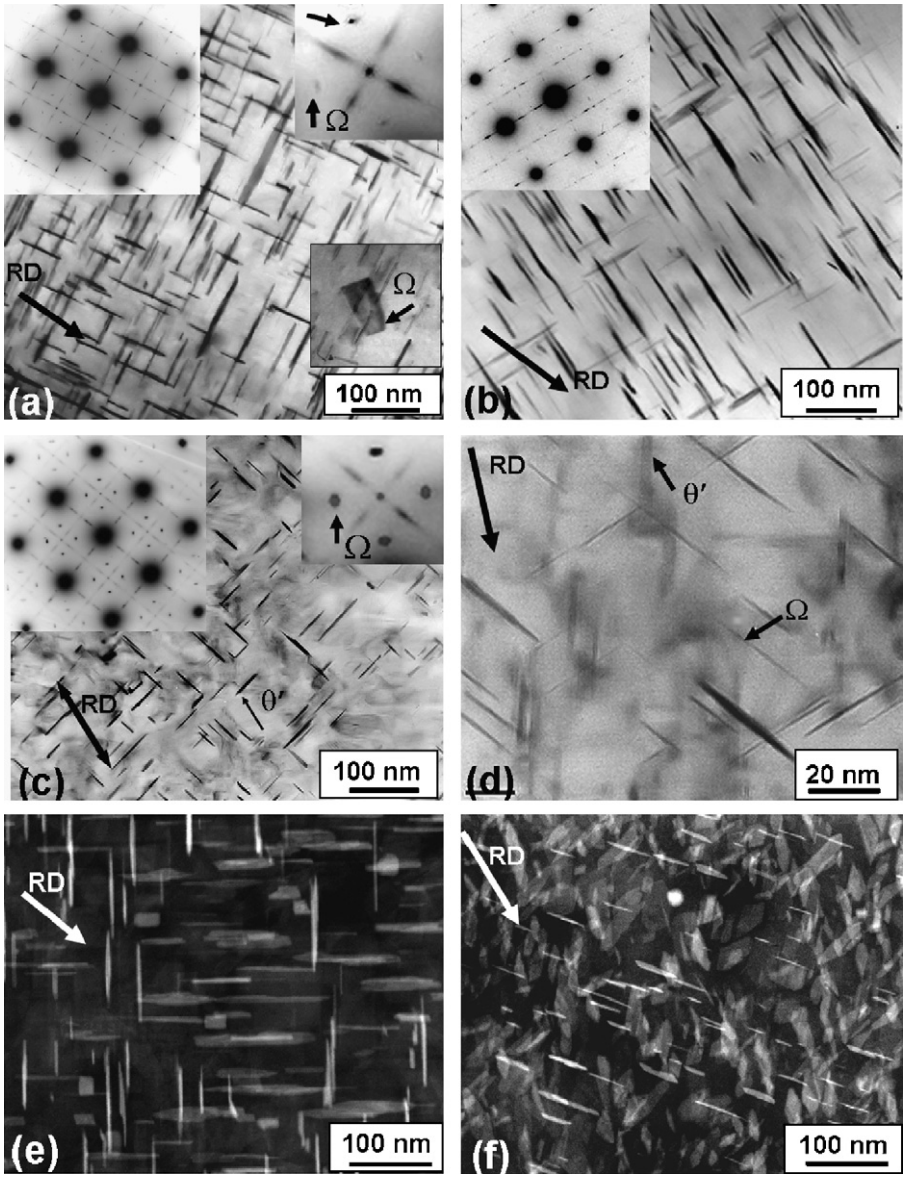

Fig. 6. Bright field TEM micrographs close to a $\langle 1\,0\,0\rangle_{Al}$ zone axis, and corresponding SAED diffraction patterns for the two alloys in their respective T8 conditions: (a) a local region where θ′ is randomly distributed and (b) stress aligned, with the $1\,1\,0_{Al}$ position enlarged, for the 2022 (Al–Cu–Mg) alloy and in (c) and (d) θ′ and Ω precipitation in the 2139 (Al–Cu–Mg–Ag) alloy (in (d) two Ω plate variants are tilted edge on using a $\langle 0\,1\,1\rangle_{Al}$ zone). In (e) and (f) a comparison is given, using dark field images, of the different densities and sizes of θ′ and Ω plates in the 2022 and 2139 alloys, respectively.

cipitate was smaller in size in the 2139 alloy and partly replaced by a spherical morphology (Fig. 10d). The appearance and nucleation behaviour of these minor constituent phases is discussed further below (see Section 3.6).

3.5. Stress alignment

The observed alignment of the GP zones, θ″ and θ′ phases in the thick plate material is most probably related to retained residual stresses that originate from differential cooling during quenching thick sections after solution heat treatment [24]. These stresses are subsequently much reduced by the stretching process and in the centre of plate materials there is typically a retained longitudinal tensile stress component, parallel to the rolling direction, of the order of 10–20 MPa [24]. As such, this stress level is quite low and would not be expected to have a strong influence on a phase's nucleation rate unless the coherency misfit of the nucleus dominates the energy barrier for nucleation and can be readily affected by interaction with the residual stress field.

In several studies the high negative plate normal coherency strains, associated with Cu GP zones, θ″, θ′ and Ω, have been shown to interact with superimposed far-field stresses, which can bias their habit plane variant selection and affect their nucleation rate and size [20–23,40]. Of these phases, the θ″, θ′ $\langle 0\,0\,1\rangle_{Al}$ habit plane family can nucleate on three possible $\{0\,0\,1\}_{Al}$ planes and the $\{1\,1\,1\}_{Al}$ habit plane Ω phase on four. A small imbalance in strain energy of the nucleus between these orientations will, therefore, bias the nucleation rate in favour of one, or more, habit plane variants. Because of the compressive misfit in the plate normal direction, the above phases will prefer to nucleate on habit planes parallel to a tensile, or perpendicular to a compressive, stress axis [20–23]. The tensile stress threshold for precipitate alignment is of the order of 20 MPa for θ′ and probably even lower for its precursors, θ″ and $\langle 0\,0\,1\rangle_{Al}$ Cu GP zones [20–23], but is a lot larger for Ω

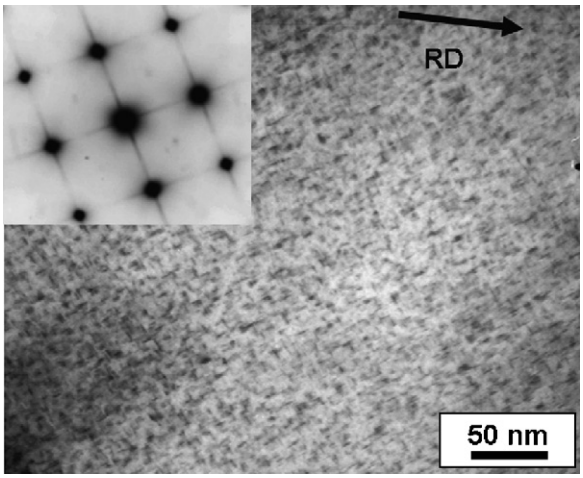

Fig. 7. Bright field TEM micrograph close to a $\langle 0\,0\,1\rangle_{Al}$ zone axis and corresponding SAED $\langle 0\,0\,1\rangle_{Al}$ diffraction pattern for the 2022 alloy, following resolution treatment using a small sample and ageing for 0.01 h at 173 °C, showing little alignment of the GP zones/θ″.

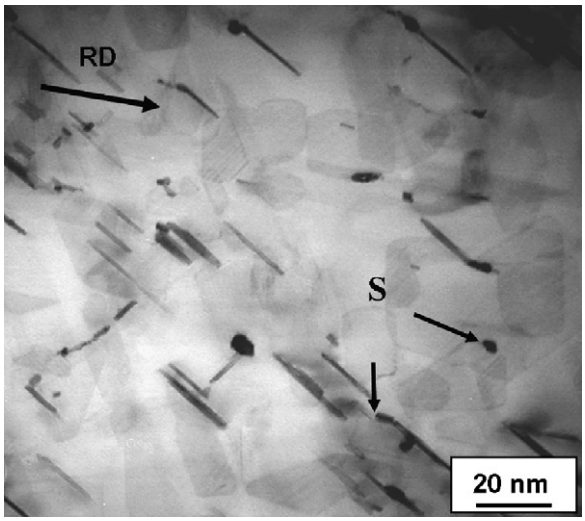

Fig. 9. Bright field TEM micrograph showing different examples of the heterogeneous nucleation of S on θ′ and Ω precipitates in the 2139 alloy after the final T8 temper. The electron beam was close to a $\langle 1\,0\,0\rangle_{Al}$ zone axis.

for which it has been reported to be at least 120 MPa [22]. In the case of Ω the higher threshold stress is possibly related to the role of Ag and Mg reducing the coherency strain during nucleation.

As a result of its higher threshold stress, preferential alignment of the Ω phase was not observed in any of the samples studied. However, in the early stages of ageing it is not surprising that the Cu GP zones, which exhibit high negative coherency strains, are preferentially aligned due to the relatively modest tensile residual stresses retained in a stretched plate (Fig. 3a). As θ″ develops from Cu GP zones this phase is also readily aligned by the residual stresses (Fig. 4a) and in the 2022 thick plate preferential alignment of the coherent θ″ was still present in the peak-aged condition. To confirm this effect was due to residual stresses, a small sample of the 2022 plate was re-solutionised and re-aged. Fig. 7 shows that following this treatment similar GP zone densities, edge on to the foil, can be seen in two $\langle 1\,0\,0\rangle_{Al}$ directions and the streaking in the diffraction pattern is symmetric, suggesting that there is now little stress biased preferential habit plane selection.

In the T8 condition, although the majority of the θ′ precipitates were randomly distributed over their available habit plane variants (Fig. 6a) some areas of local alignment parallel to the longitudinal tensile residual stresses in the plate were still found, shown

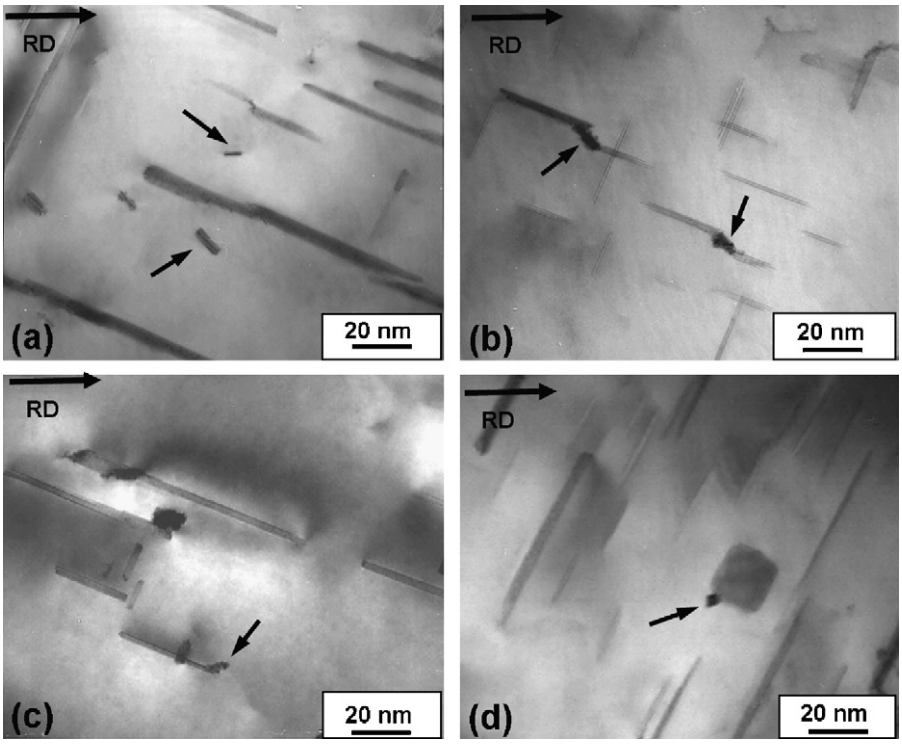

Fig. 8. Bright field TEM micrographs showing different examples of the heterogeneous nucleation of S precipitates present in the 2022 T8 alloy (a) at matrix dislocations, (b) between two θ′ plate precipitates, (c) at the interface of a single θ′ plate precipitates and (d) at the interface of a σ phase precipitate. The electron beam was close to a $\langle 1\,0\,0\rangle_{Al}$ zone axis.

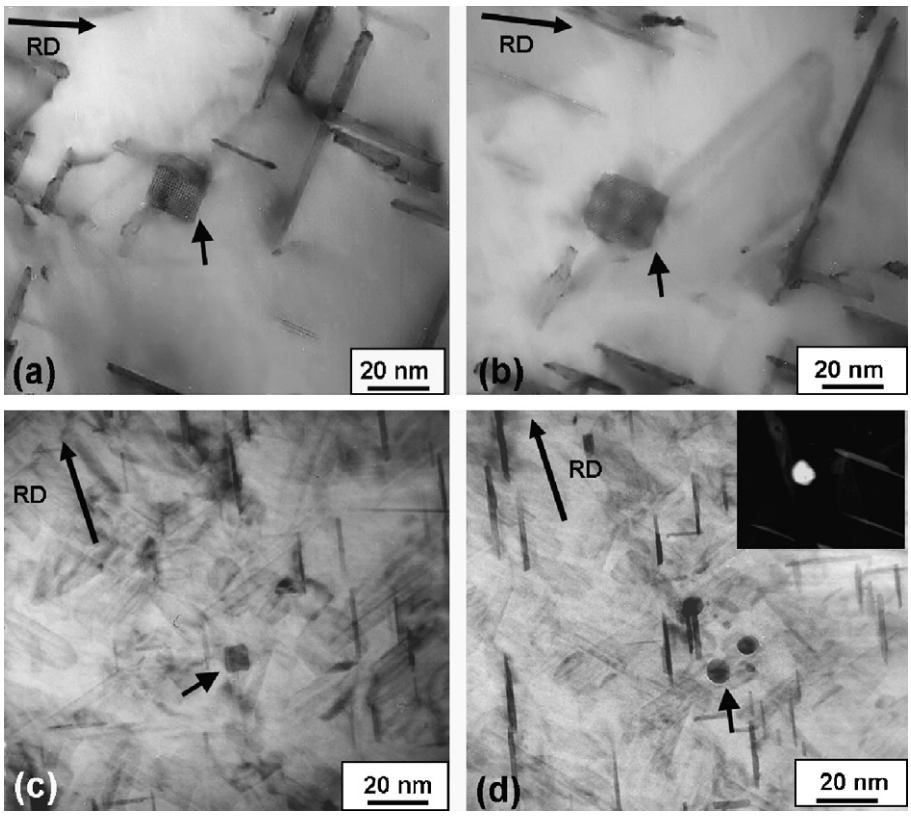

Fig. 10. Bright field TEM micrographs showing the σ phase with a cubic morphology precipitating at the edges of θ′ and Ω plate precipitates in the 2022 alloy, (a) and (b), and far smaller σ precipitates with a cubic, or spherical, morphology in the Ag containing 2139 alloy, (c) and (d). The HAADF insert image in (d) reveals a rounded face from the side closest to the Ω plate. The electron beam was close to a $\langle 1\,0\,0\rangle_{Al}$ zone axis in all cases.

in Fig. 6b. These different areas probably correspond to regions of high and low dislocation density in the stretched alloy, with θ′ being less sensitive to a weak residual stress when nucleated within the intense local strain field surrounding a dislocation line. From careful observation of the images in Fig. 6b, it can be detected that there is a difference in precipitate length between the regions with randomly distributed and aligned plates. In the ⟨0 0 1⟩ TEM images both the θ′ edge on plate variants in the non-aligned case had almost identical lengths, with $d_{||} = 70$ nm, $d_{\perp} = 69$ nm for the variants closest to parallel and normal to the rolling dictation, respectively. However, in the areas of local preferential alignment, the dominant plate variant closest to being parallel to the RD direction was longer, $d_{||} = 85$ nm, compared to an average length for the precipitates normal to RD, of $d_{\perp} = 66$ nm. A relative increase in length of the favoured habit plane plate variant has been previously noted during stress ageing by Zhu and Starke [21], although here this effect is complicated by the lower dislocation nucleation site density in the aligned volumes.

Unfortunately, the 2139 alloy was not available in a 40 mm plate form to confirm if similar phenomena could be observed with the θ″ and θ′ phases in this alloy. However, because the response of the material in this case was dominated by Ω precipitation, stress orientation during ageing would not be expected to have a very significant effect on its T8 microstructure.

3.6. Minor phases

Although neither the S nor σ phase, will have a significant impact on the mechanical properties of the two alloys, owing to their very low volume fraction, it is still interesting to consider in more detail their nucleation behaviour in association with the dominant age hardening phases and subtle differences in their morphology in the two alloys, as a function of the addition of silver.

3.6.1. S phase

The S (or S′) phase was observed to appear with a similar very small volume fraction in the final T8 microstructures of the two alloys (<0.1%). Lath-shaped S precipitates were first observed to form after 6–8 h ageing at temperature in the 2022 alloy (173 °C) and after 4–6 h in 2139 (175 °C), prior to the presence of the σ phase (Fig. 8). From careful observation of TEM images (Fig. 8), the S phase was found to nucleate heterogeneously either on dislocations (Fig. 8a), between two θ′ precipitates (Fig. 8b), or sometimes also at the interface of a single θ′ plates (Fig. 8c). Later on in the ageing sequence, S was also found to nucleate at the interface of the σ phase (Fig. 8d). TEM evidence further showed that the S phase nucleated on the Ω phase in the 2139 alloy (Fig. 9). This may also occur in the 2022 alloy. However, the low volume fraction of the Ω phase in this material made observation difficult. Pre-precipitation of θ′ and Ω therefore appears to encourage the nucleation of S. In the T8 condition S was most commonly seen with a lath morphology.

There is some discussion in the literature concerning the transition series in alloys where S is the dominant age hardening phase (i.e. alloys like 2024 with Cu:Mg ratios closer to 1) [7,16,41–43]. In the alloys considered, which had low Mg levels, the debated S″/GPB2 phase is unlikely to be present after the T8 ageing treatment. A lathe morphology slightly distorted semicoherent variant of the S phase (or S′) with a $\{0\,1\,2\}_{Al}$ habit plane has been widely reported to prefer to nucleate heterogeneously at dislocations [7,16,41–43]. Semicoherent S has also been reported to nucleate at interfaces with other phases [7]. A second variant of S with a slightly different orientation relationship has been proposed to form in alloys at higher ageing temperatures that have not been pre-deformed [12]. Although to date we have not attempted to discriminate between these two possibilities, this variant is unlikely to be relevant here. With a low Mg level, the chemical driving force for

S precipitation will be very small, making its nucleation extremely sensitive to the effectiveness of a given heterogeneous nucleation site in terms of; the reduction in strain energy that can be achieved by the nucleus, lowering of surface energy through wetting an interface, and any local increase in Mg supersaturation that may result from a prior precipitate reaction. This may explain why S was often found in association with the θ′ and Ω phases (Fig. 8), which have substantial coherency strain fields, and where Mg is known to segregate to the Ω phase interface. During growth rejected Mg could also potentially build up ahead of the Al_2Cu θ′ interface. At other nucleation sites, such as the σ phase, which also requires Mg, nucleation of the S phase nucleus may benefit from a reduction in strain energy.

3.6.2. σ phase

The σ phase only appeared late in the ageing sequence with a very low volume fraction (<0.1%) and was also found to exhibit a relationship with other precipitates in the matrix. In the 2022 alloy, σ had the characteristic cuboidal morphology previously reported [7,37–39]. In Fig. 10a a σ precipitate can be seen to coexist with a θ′ and Ω precipitate, where it probably nucleated. The size of the σ cubes varied from 15 nm to 20 nm and similar dimensions and nucleation sites associated with prior phases have been observed by Lumley and Polmear for a comparable ageing treatment in an Al–5.8%Cu–0.45%Mg–0.45%Ag alloy [7].

In the 2139 material, although cubic morphology σ phase precipitates were observed in the T8 condition (Fig. 10c), they were significantly smaller than in the 2022 alloy (~7–10 nm). Furthermore, an additional precipitate type was seen similar in appearance to σ, but with an approximately spherical morphology (Fig. 10d). These spherical precipitates also nucleated at the interface of Ω and θ′ plates (Fig. 10c) and had the same composition as the cubic σ phase. These findings suggest that the spherical-shaped precipitate is the same σ phase, but it has a modified morphology. This could be because it has not grown large enough to become facetted, but it is also more likely to appear spherical if it initially grows with $\{1\,1\,1\}_{Al}$ facets from nucleation between Ω plates (as reported by Lumley and Polmear [7]) which predominate in the 2139 alloy.

Alternatively, since Ag is known to segregate to the interface of the Ω phase, and reduce its coherency strains, the change to a spherical morphology could potentially be explained by segregation of Ag to the interface of σ, reducing its misfit strain, or increasing the isotropy of its interfacial energy. To investigate this possibility further, STEM-EDS line scans were performed across the σ phase in both alloys. The STEM line scan, shown in Fig. 11a for the Ag-free 2022 alloy, traverses across a σ particle and a θ′ plate. As the probe crosses over the cuboidal σ particle, the Cu and Mg levels rise to ~14 and 3 wt.%, respectively, and for obvious reasons no Ag can be detected. In the 2139 Ag containing alloy (Fig. 11b), the line scan extends through a small spherical morphology σ precipitate and a tilted Ω plate (~55° to vertical when viewed close to a $\langle 0\,0\,1\rangle_{Al}$ zone axis). Due to overlap of the K_α peaks for Mg with Al, the close proximity of other Cu containing particles, and the sensitively to errors in ZAF correction without accurate knowledge of the foil thickness, it is not surprising that, although similar in each alloy, the Mg to Cu ratio is lower than would be expected from the reported σ phase stoichiometry [37–39]. Interestingly, in the 2139 sample line scan data a peak in Ag can be observed associated with the σ particle's interface of ~3 wt.%. and a peak of similar magnitude can also be observed when the line scan extends across the Ω precipitate.

It has been proposed that the presence of σ phase in Al–Cu–Mg alloys [37–39,44] depends on a minimum level of Mg, which is incorporated into the phase, as well as Si, which acts as a nucleant, although other researchers have reported that Ag may have a similar effect [45]. The findings here suggest that neither of these

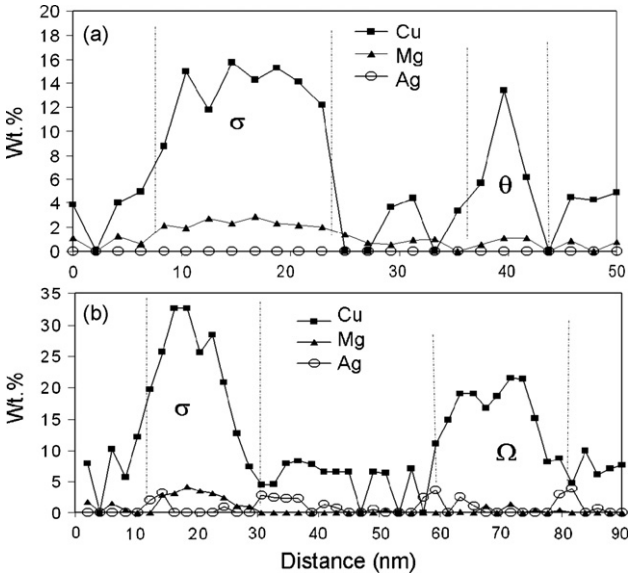

Fig. 11. EDS STEM line scans across (a) a cubic σ precipitate and vertical θ′ plate present in the Ag-free 2022 alloy, and (b) a spherical σ precipitate and a tilted Ω plate present in the Ag-containing 2139 alloy, both in their respective T8 tempers.

arguments is the sole reason for σ precipitation, since the alloys investigated had a low Mg level, very low Si content (0.02 wt.%) and the 2022 alloy does not contain any Ag. Clearly a minimum Mg level is necessary, but this must be lower than previously reported. The results showed that the σ phase was the last phase to form and this occurs primarily by nucleation in between Ω and θ′ precipitates, which must, therefore, appear first. Lumley and Polmear [7] first observed this interaction and also proposed that at least one of the chamfered edges of the cuboid σ phase, lies on the face of an Ω plate precipitate. The σ phase has been reported to have a negative misfit with the matrix of approximately −2.8% [37–39] and thus probably prefers to nucleate at the interface of a plate to reduce its strain energy. It has been further suggested by Lumley and Polmear [7] that σ utilises the Mg atoms locally enriched in the matrix at the surface of the Ω phase and the availability of Mg solute segregated to the interface of Ω and θ′ plates could also affect the nucleation of the σ phase on their faces.

The change in morphology of the σ phase from cuboidal to a more spheroidal shape in the presence of Ag, in low Mg content alloys, has not been previously discussed and, from the results presented above, appears to be partly due to a refinement in the size of the σ phase in the 2139 alloy and a greater tendency for Ω-assisted nucleation, which leads to $\{1\,1\,1\}_{Al}$ faceting. However, the observed segregation of Ag to the interface will also relax the coherency misfit, potentially making the morphology adopted less sensitive to the softer $\langle 0\,0\,1\rangle$ direction elastic anisotropy in the Al matrix.

4. Conclusions

The precipitation behaviour during artificial ageing to a T8 temper of two new commercial 2xxx aluminium alloys, 2022 and 2139, with a high Cu:Mg ratio has been investigated in more detail than previously reported. The main difference between the two compositions was the addition of ~0.3% silver and a slightly higher Mg level in 2139.

When aged to the T8 temper, the Ag-free 2022 alloy was found to contain, θ′, Ω, S, and σ phase; with θ′ the dominant strengthening phase, and very small volume fractions of S and σ. To date Ω has not been previously reported in 2xxx Al-alloys with such a low Mg level. The addition of a small concentration of silver in 2139

greatly increased the age hardening response and radically affected the microstructure evolution, inhibiting the formation of Cu {0 0 1} GP zones and θ″, by the promotion of Mg–Ag and Mg–Ag–Cu co-clusters, and largely replacing the θ′ phase with Ω. In the T8 temper the 2139 alloy also contained θ′, S, and σ phase, but was dominated by Ω with a low θ′ content and similar very small volume fractions of S and σ.

The S phase was found to nucleate heterogeneously at dislocations, between Ω and θ′ plates, as well as at the interface with the σ phase. The σ phase was found to nucleate at the interface of, and often between, Ω and θ′ plates and have a reduced size in the 2139 alloy. Evidence was found that Ag maybe incorporated into the interface of the σ phase.

While low, the remaining tensile residual stresses present in the centre of thick plate material, after stretching, were found to be sufficient to bias the nucleation of Cu GP, zones/θ″, and, to some extent, θ′, on habit plane variants aligned preferentially in the rolling direction. A similar effect was not observed for Ω because of its higher stress threshold for biased nucleation.

Acknowledgements

This research was funded through AGEFORM “Ageformable Panels for Commercial Aircraft” in the European Commission’s framework programme (G4RD-CT-2002-00743) and the University of Manchester EPSRC Light Alloys Portfolio Partnership (EP/D029201/1) in collaboration with Alcan and Airbus UK.

References

[1] T.J. Warner, Mater. Sci. Forum 519–521 (2006) 1271.
[2] A. Cho, B. Bes, Mater. Sci. Forum 519–521 (2006) 603.
[3] F. Eberl, Ageform, Aerodays, Vienna, 2006.
[4] I.J. Polmear, G. Pons, Y. Barbaux, H. Octor, C. Sanchez, A.J. Morton, W.E. Borbidge, S. Rogers, Mater. Sci. Technol. 15 (1999) 861.
[5] S.P. Ringer, W. Yeung, B.C. Muddle, I.J. Polmear, Acta Metall. Mater. 42 (1994) 1715.
[6] C.R. Hutchinson, X. Fan, S.J. Pennycook, G.J. Shiflet, Acta Mater. 49 (2001) 2827.
[7] R.N. Lumley, I.J. Polmear, Scr. Mater. 50 (2004) 1227.
[8] A. Garg, J.M. Howe, Acta Metall. Mater. 39 (1991) 1939.
[9] B.M. Gable, G.J. Shiflet, E.A. Starke Jr., Scr. Mater. 50 (2004) 149.
[10] B.C. Muddle, I.J. Polmear, Acta Metall. 37 (1989) 777.
[11] I.J. Polmear, R.J. Chester, Scr. Metall. 23 (1989) 1213.
[12] L. Reich, M. Murayama, K. Hono, Acta Mater. 46 (1998) 6053.
[13] S.P. Ringer, K. Hono, I.J. Polmear, T. Sakurai, Acta Mater. 44 (1996) 1883.
[14] S.P. Ringer, K. Hono, I.J. Polmear, T. Sakurai, Appl. Surf. Sci. 94/95 (1996) 253.
[15] S.P. Ringer, T. Sakurai, I.J. Polmear, Acta Mater. 45 (1996) 3731.
[16] S.C. Wang, M.J. Starink, Acta Mater. 55 (2007) 933.
[17] J.F. Nie, B.C. Muddle, Scr. Mater. 42 (2000) 409.
[18] H. Hargaret, M.T. Lyttle, E.A. Starke, Mater. Sci. Eng. A 257 (1998) 87.
[19] P.B. Prangnell, W.M. Stobbs, Proceedings of the 12th Risø International Symposium, Roskilde, Denmark, Risø, 1991, p. 603.
[20] T. Eto, A. Sato, T. Mori, Acta Metall. 26 (1978) 499.
[21] A.W. Zhu, E.A. Starke Jr., Acta Mater. 49 (2001) 2285.
[22] B. Skrotzki, G.J. Shiflet, E.A. Starke, Metall Trans. A 27A (1996) 3431.
[23] D. Bakavos, P.B. Prangnell, R. Dif, Mater. Sci. Forums 28 (2004) 124.
[24] M.B. Prime, M.R. Hill, Scr. Mater. 46 (2002) 77.
[25] I.J. Polmear, Trans. AIME 230 (1964) 1331.
[26] J.T. Vietz, I.J. Polmear, J. Inst. Met. 97 (1966) 87.
[27] J.L. Murray, Int. Met. Rev. 30 (1985) 211.
[28] E. Matsubara, J.B. Cohen, Acta Metall. 31 (1985) 2129.
[29] W.M. Stobbs, G.R. Purdy, Acta Metall. 26 (1978) 1069.
[30] R.N. Lumley, A.J. Morton, I.J. Polmear, Acta Mater. 50 (2002) 3597–3608.
[31] J.M. Silcock, J. Inst. Met. 89 (1961) 203–210.
[32] V.A. Philips, Acta Metall. 23 (1975) 75.
[33] U. Dahmer, K.H. Westmacott, Phys. Status Solidi A 80 (1983) 249–262.
[34] G.W. Lorimer, R.B. Nicholson, The mechanism of Phase Transformations in Crystalline Solids, Monograph, vol. 33, Inst. Metals, 1969, p. 36.
[35] G.W. Lorimer, Proceedings of the Fourth European Regional Conference of Electron Microscopy, Tipografia Pouglotta, Vaticana, Rome, 1967, p. 249.
[36] T.J. Konno, M. Kawasaki, K. Hiraga, Philos. Mag. B 81 (2001) 1713.
[37] R.D. Schueller, F.E. Wawner, A.K. Sachdev, J. Mater. Sci. 29 (1994) 239.
[38] R.D. Schueller, F.E. Wawner, A.K. Sachdev, J. Mater. Sci. 29 (1994) 424.
[39] R.D. Schueller, A.K. Sachdev, F.E. Wawner, Scr. Mater. 27 (1992) 1289.
[40] D. Bakavos, P.B. Prangnell, B. Bes, F. Eberl, S. Gardiner, Mater. Sci. Forum 519–521 (2006) 407.
[41] A. Charai, T. Walther, C. Alfonso, A.M. Zahra, C.Y. Xahra, Acta Mater. 48 (2000) 2751.
[42] A.K. Gupta, P. Gaunt, M.C. Chaturvedi, Philos. Mag. A 55 (1987) 375.
[43] V. Radmilovic, R. Kilas, U. Dahmen, G.J. Shiflet, Aca Mater. 54 (1999) 3987.
[44] A.K. Mukhopadhyay, Metall. Trans. A 33 (2002) 3635.
[45] Q. Li, F.E. Wawner, J. Mater. Sci. 32 (1997) 5363.